

Chapter 2

Equivalent Circuit

2.1 Equivalent Circuit Model

A particularly attractive feature of such geometries is that it is possible to fabricate an efficient cell using ultra-thin organic thin films (lower than 50 nm), and thereby lead to high filling factors due to decreased recombination (Reprinted with permission from [1], Copyright (2011) by The American Physical Society), [2–4] Further, due to the well-defined mode structure of many of these geometries, there is the possibility of effectively utilizing frequency conversion schemes. Because of the long optical path in the fiber, a frequency convertor can play an effective role in doubling high energy photons to improve current. However, there are still several problems that must be overcome. We have reported that the open-circuit voltage (V_{oc}) tends to decrease in Optical Confinement Geometry Organic Photovoltaics (OCGOPV) geometries [5, 6]. In that earlier work [5], we defined two “active” areas of the general three dimensional geometry as Fig. 2.1a shows: the “Current Active Area” (CAA) is the area from which current is collected and the “Illumination Active Area” (IAA) is the area of illumination of the structure [5]. These are a distinctive feature of any OCGOPV. Essentially for the planar cell, IAA equals CAA, but in the OCGOPV the CAA is much greater than the IAA. In other words, the flux entering the aperture (IAA) is spread over a much larger area within the cell (the CAA) leading to a lower optical intensity on CAA like an inverse concentrator. Because light is generally partitioned into modes of the “confining cavity,” the optical intensity in an OCGOPV is typically heterogeneously distributed across the CAA (HeOI), differing from the homogeneous optical intensity (HoOI) in planar OPV. The heterogeneous distribution in OCGOPVs can be simulated by the ray tracing model we reported [7] as shown in Fig. 2.1b. If this power heterogeneity becomes too great, a loss in V_{oc} will occur for the device. In this section, we examine the effects of optical heterogeneity on a model OCGOPV using a composite equivalent circuit analysis.

To understand the performance of an OCGOPV, it is necessary to know the connections between their electrical and optical characteristics. First, as shown in

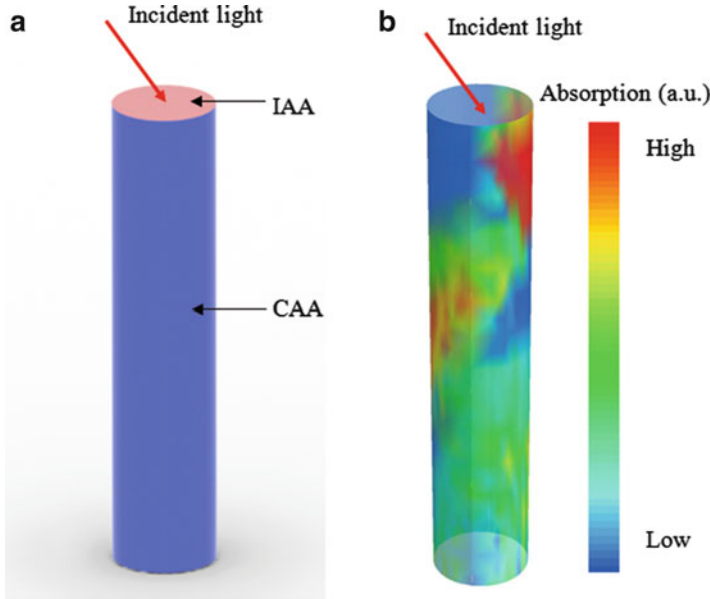


Fig. 2.1 (a) IAA and CAA are represented as *pink* area at the top and *blue* area round the fiber. (b) Heterogeneous absorption distribution through inner surface in OCGOPVs is simulated by a ray tracing model [7]. The legend at the *right* represents the absorption level at inner surface

Fig. 2.2a, we take a small piece from a whole OCGOPV (a.1) as one *subunit* (a.2) and treat it like a planar solar cell (a.3). For each *subunit* in (a.2), when very small, we may assume it fits planar cell theory. In Fig. 2.2b, the equivalent circuit of planar cell is described by J-V characteristics expressed by the generalized Shockley equation [8–10].

$$J = \frac{R_p}{R_s + R_p} \left\{ J_s \left[\exp \left(\frac{e(V - JR_s)}{n_D k_B T} \right) - 1 \right] + \frac{V}{R_p} - J_{ph} + J_{Rec.} \right\} \quad (2.1)$$

Where, n_D is the diode ideality factor, J_s is the reverse saturation current, and $J_{Rec.}$ is represented by the current source, which counteracts the photocurrent density J_{ph} [11–13]. Due to lower carrier mobility in polymers generally [14–16], the main factors influencing the recombination rate $r_{Rec.}$ are thickness of polymer, the temperature and the fabrication procedure/polymer processing used. For very thin films of bulk heterojunction polymer blends, the influence of $r_{Rec.}$ on J_{sc} can be safely ignored [2].

To account for heterogeneity in the OCGOPVs, the model must consist of many OPV *subunits* with different performances, as shown in Fig. 2.2c. They absorb different photon numbers to contribute many j_i , and each generates a different v_i .

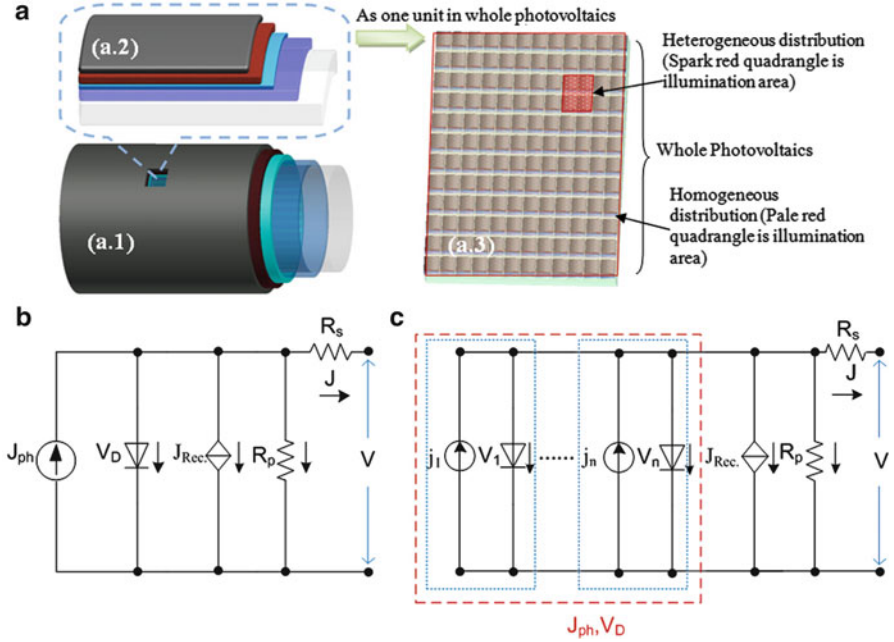


Fig. 2.2 (a) From (a.1) to (a.3), our model divides the OCGOPV into *subunits*, and then connects them as a planar photovoltaics. In (a.3), illumination across the *subcells* is heterogeneously distributed due to the mode structure of the waveguide. (b) The equivalent circuit of conventional planar OPV. J_{ph} , J_{Rec} , V_D , R_s , and R_p are photocurrent source, recombination, diode voltage, series resistances and parallel resistances, respectively. J and V are the output current density and voltage of OPV. (c) The equivalent circuit of the OCGOPVs composed of unit *subcells*

The contributions from the individual cells are summed to provide a whole J_{ph} and V_D as show below.

$$J_{ph} = \frac{1}{n} \sum_{i=1}^n j_i = \frac{1}{n} \sum_{i=1}^n \int \frac{q\lambda}{hc} \eta(\lambda) Q_i(\lambda) d\lambda \quad (2.2)$$

Where, $Q_i(\lambda)$ is the spectral irradiance on the active area from the incident light at each *subunit*, which can be obtained by a 3D fiber-cell model based on ray tracing [7] coupled with a transfer matrix method which accounts for the materials absorption properties [2, 3, 17, 18]. In Eq. 2.2, h , c , q , and λ are the Planck's constant, light speed, electron charge, and wavelength. $\eta(\lambda)$ is the external quantum efficiency of wavelength λ . From Eq. 2.1, when $J = 0$, the open-circuit voltage $V_{oc} = V = V_D$. Also since $J_s R_p \gg V_{oc}$ [12], Eq. 2.2 can be simplified as:

$$V_{oc} = \frac{n_D k_B T}{q} \ln \left(\frac{(R_p + R_s) J_{ph}}{J_s R_p} + 1 \right), J_{ph} = \frac{1}{n} \sum_n j_i \quad (2.3)$$

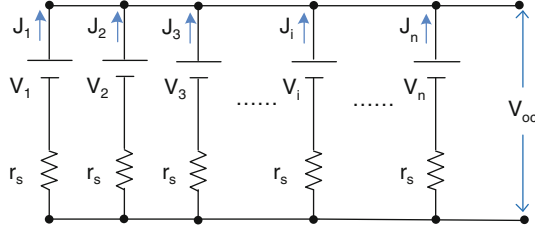


Fig. 2.3 The circuit of superimposed V_i to whole voltage V_{oc}

Equation 2.3 represents the case of homogeneous illumination when all j_i are equal.

In Fig. 2.3, the superimposed voltage V_{oc} is described as the average of all voltage of *subcells* cells, as shown in Eqs. 2.4 and 2.5.

$$0 = \sum_n j_n = \sum_n \frac{V_{oc} - V_i}{r_s} \quad (2.4)$$

Thus,

$$V_{oc} = \frac{\sum_n V_i / r_s}{\sum_n 1 / r_s} = \sum_n V_i \quad (2.5)$$

$$V_{oc} = \frac{1}{n} \sum_n V_i \quad (2.6)$$

$$V_i = \frac{n_D k_B T}{q} \ln \left(\frac{(R_p + R_s) j_i}{J_s R_p} + 1 \right) \quad (2.7)$$

Therefore, when the optical intensity is heterogeneous, i.e. each *subunit* cell absorbs different light fluxes and contributes various voltages, their superimposed voltage V_{oc} is described as the average of all voltage of unit *subcells* in Eq. 2.6 [19].

When j_i is constant and equals the average current density of the whole cell, Eq. 2.7 becomes Eq. 2.3 of the homogeneous case. Actually, j_i is a function of position x , namely $j_i = j(x)$, which is related to optical distribution by Eq. 2.2. We can use the method of calculus of variations to express the relationship of V_{oc} with optical distribution $j_i(x)$. We assume

$$V_{oc} = \frac{1}{n} \sum_n a \ln(b j_i(x) + 1) \quad (2.8)$$

$$\text{where } \Psi a = \frac{n_D k_B T}{q}, b = \frac{R_p + R_s}{J_s R_p} \quad (2.9)$$

Equation 2.8 is rewritten as an integral.

$$V_{oc} = \frac{1}{n} \sum_n a \ln(b j_i(x) + 1) = \int_0^{x_0} \frac{a}{x_0} \ln(b j(x) + 1) dx \quad (2.10)$$

Where, x_0 is the area of whole cell. And we assume the total current is constant, and the range of x_i is invariant, i.e. the area x_0 is constant. Then, the effect of distribution of $j(x)$ can be studied in terms of the definition of functional derivative

$$\delta F = \int d^3r d \frac{\delta F}{\delta n(r)} \delta n(r) \quad (2.11)$$

$$\begin{aligned} \delta V_{oc} &= \int dx d \frac{\delta V_{oc}}{\delta j(x)} \delta j(x) \\ &= \frac{a}{x_0} \int_0^{x_0} \{ \ln[bj(x) + \delta j(x)] + 1 \} - \ln(bj(x) + 1) \} dx \\ &= \frac{a}{x_0} \int_0^{x_0} \{ \ln(bj(x) + 1) + \frac{b\delta j(x)}{bj(x) + 1} - \ln(bj(x) + 1) \} dx \\ &= \frac{a}{x_0} \int_0^{x_0} \frac{b\delta j(x)}{bj(x) + 1} dx \end{aligned} \quad (2.12)$$

The kernel of that integral determines the influence of the variation of distribution $j(x)$. By put Eq. 2.9 and the following parameters into this kernel.

$$\begin{aligned} T &= 300K \\ n_D &= 1 \\ k_B &= 1.3806505 \times 10^{-23} J/K \\ q &= 1.6 \times 10^{-19} C \end{aligned} \quad (2.13)$$

Also, when j_s is much less than $j(x)$, the kernel becomes

$$\begin{aligned} \frac{a}{x_0} \frac{b}{bj(x) + 1} &= \frac{0.026V}{x_0} \frac{r_p + r_s}{j_s r_p + j(x)(r_p + r_s)} \\ &\approx \frac{0.026V}{x_0} \frac{r_p + r_s}{j(x)(r_p + r_s)} \\ &= \frac{0.026V}{x_0} \frac{1}{j(x)} \end{aligned} \quad (2.14)$$

Where, x_0 can be assumed as a unit area, $j(x)$ can be regard as the average current density in homogeneous, and $\delta j(x)$ is the perturbation in heterogeneous distribution. This means that the heterogeneous illumination can be described by the homogeneous model if the ratio $\delta j(x)/j(x)$ is of the same order of magnitude. Thus, Eq. 2.12 becomes

$$\delta V_{oc} \approx \int_0^{x_0} \frac{0.026V}{x_0} \frac{\delta j(x)}{j_{HoD}} dx = \frac{0.026V}{x_0 j_{HoD}} \int_0^{x_0} \delta j(x) dx \quad (2.15)$$

Since the total current is constant, i.e., the integral of the variation of current density $j(x)$ is 0, $\delta V_{oc} = 0$.

In addition, the variance of light distribution is used to estimate the upper bound of the V_{oc} in homogeneous illumination and that in heterogeneous illumination.

As Eq. 2.8 shown, V_{oc} is represented as

$$V_{oc} = \frac{1}{n} \sum_{i=1}^n a \ln(bj_i + 1) = a \ln b + a \frac{1}{n} \sum_{i=1}^n \ln(P_i) \quad (2.16)$$

Where

$$P_i = j_i + \frac{1}{b} \quad (2.17)$$

Thus,

$$e^{V_{oc}} = e^{a \ln b} \left(\prod_{i=1}^n P_i \right)^{a/n} \quad (2.18)$$

In terms of a theorem [20] related to arithmetic mean geometric mean in Eq. 2.19, it gives a lower bound of Eq. 2.18 as Eq. 2.21 shown, which is related with the variance and average of P_i .

$$\prod_{i=1}^n x_i^{1/n} \geq \bar{x} - \frac{1}{2u} \sum_{i=1}^n \frac{1}{n} (x_i - \bar{x})^2 \quad (2.19)$$

$$x_i \in [u, v] \quad (2.20)$$

$$e^{V_{oc}} = e^{a \ln b} \left(\prod_{i=1}^n P_i \right)^{a/n} \geq e^{a \ln b} \left(\bar{P} - \frac{1}{2u} s \right)^a \quad (2.21)$$

Where

$$s = \frac{1}{n} \sum_{i=1}^n P_i^2 - \bar{P}^2 = \sigma \quad (2.22)$$

$$\bar{P} = \frac{1}{n} \sum_{i=1}^n P_i = \mu + \frac{1}{b} \quad (2.23)$$

$$\sigma = \frac{1}{n} \sum_{i=1}^n j_i^2 - \mu^2 \quad (2.24)$$

$$\mu = \frac{1}{n} \sum_{i=1}^n j_i \quad (2.25)$$

Then, the upper bound of V_{oc} is written as:

$$V_{oc} \geq a \ln b + a \ln \left(\bar{P} - \frac{1}{2u} s \right) = a \ln b + a \ln \left(\mu + \frac{1}{b} - \frac{1}{2u} \sigma \right) \quad (2.26)$$

The homogeneous illumination is represented as when distribution variance $\sigma = 0$ and the V_{oc} is written as Eq. 2.27 that corresponds with the V_{oc} formula of homogeneous case in manuscript.

$$V_{oc-homo} = a \ln b + a \ln \left(\mu + \frac{1}{b} \right) \quad (2.27)$$

Finally, the expected difference of homo-case and hetero-case to V_{oc} is obtained by Eq. 2.28.

$$V_{oc-homo} - V_{oc-heter} \leq a \ln \left(\frac{2u(1 + b\mu)}{2u(1 + b\mu) - b\sigma} \right) \quad (2.28)$$

Since the average power μ of homo-case and hetero-case are the same, only the variance σ determines this upper bound in Eq. 2.28. In addition, for most polymer devices [21] and for most common distribution, $2u(1 + b\mu) \gg b\sigma$, therefore $V_{oc} - V_{oc-homo} \sim 0$, i.e., homogeneous illumination and heterogeneous illumination show a similar impact on V_{oc} . Beside the upper bound, we will give an accurate prediction in the next step research.

2.2 Heterogeneous Illumination

Now, we expand this principle to the architecture of a real device as shown in Fig. 2.4. First, it is imperative to know which variables are important and how they influence the optical power distributions, so we consider a specific geometry such as one single tube waveguide. As we have recently shown for fibers, which also holds true for tubes [7], the ratio of length to diameter can influence light absorption in the OCGOPVs, and as noted, this geometry also leads to a heterogeneous distribution of optical power in inner surface of this specific geometry. Further, there is a strong dependence of short-circuit current J_{sc} , on the incident angle at which the illumination is coupled. The optimum incident angle depends on this ratio of length to diameter of the structure Fig. 2.5 [7, 22].

Tube-based solar cell is an extended fiber device with a hemisphere bottom. They were fabricated on glass tubes with one end closed in a hemispherical cap (Chemglass, 1 mm I.D). The ITO films with a thickness of 100 nm were deposited on these substrates by radio frequency magnetron sputtering (BOSCH) from an ITO target. (Depositing 100 nm ITO per 120° rotation, for three times.) The substrates

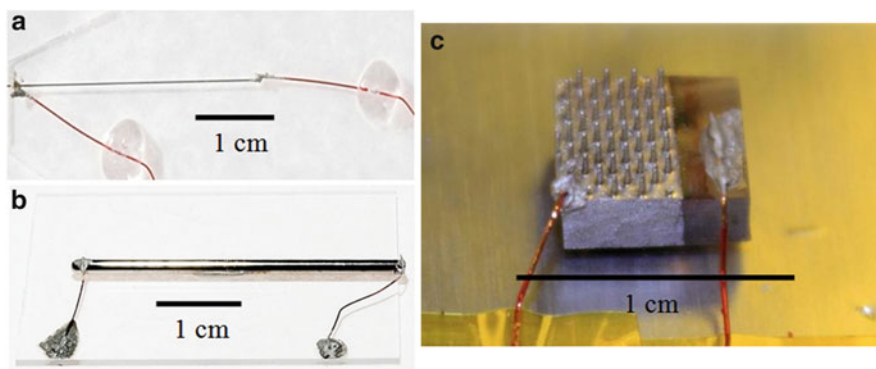


Fig. 2.4 (a) Fiber-based solar cell. (b) Tube-based solar cell. (c) Aligned plastic fiber cell with different diameter and length

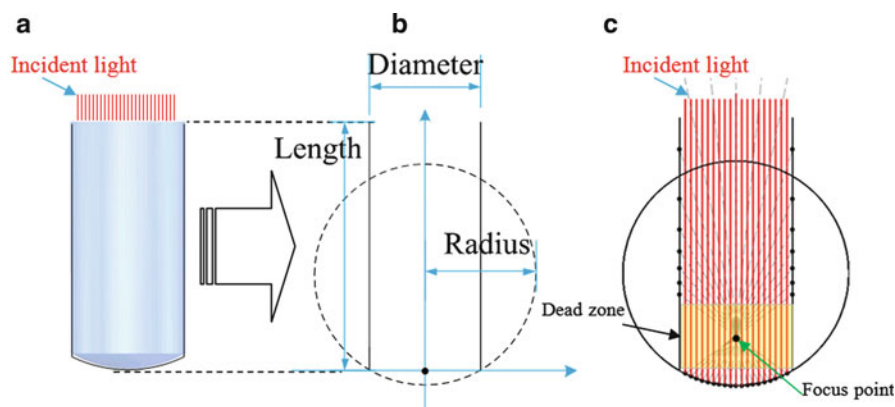


Fig. 2.5 (a) A OCGOPV with a given curvature cap at the bottom. (b) Light path in longitudinal section of (a). A beam of light (red lines, distance to y axis is x) enters into the tube (length h) and reflects at points (x_1, y_1) on bottom of curvature radius r , then reach the inner surface (x_2, y_2) . (c) There is a “dead zone” near bottom, where no light shines. Red lines (solid lines) are incident light paths; and gray lines (dashed lines) are reflected light paths

were then exposed to ozone for 90 min (rotating the tubes three times every 30 min). Subsequently, the buffer layer and absorber layer were added by dip coating. Poly (3,4-ethylenedioxythiophene)-poly(styrenesulfonate) (PEDOT:PSS, Clevis P, the film thickness is ~ 40 nm), and poly 3-hexyl thiophene:phenyl- C_{61} -butyric acid methyl ester (P3HT:PCBM = 1:0.8 in WT in chlorobenzene, of 15 mg/ml P3HT for planar cell and 5 mg for tube devices) were deposited on the tube substrate. Finally, Al electrodes were deposited via thermal evaporation at the pressure of 10^{-6} torr. Similarly, planar devices were fabricated using spin coating, for comparison. Both devices were lightly annealed ($\sim 100^\circ\text{C}$ for 5 min).

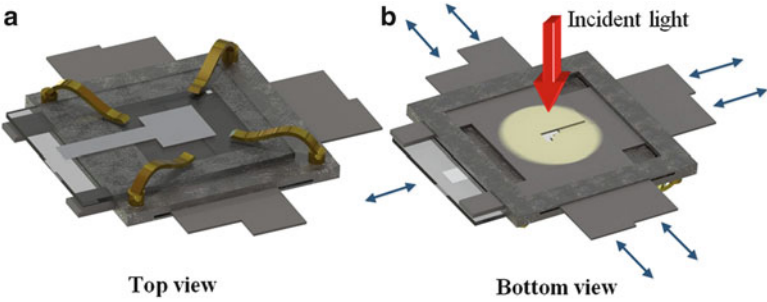


Fig. 2.6 A tool for measuring heterogeneous distribution of solar light in a subunit of a planar device. Solar light comes from the bottom (*Red arrow (light arrows)* in (b) shows the direction of solar light), and goes through the aperture hole for which the size could be adjusted by four panels. (*Blue arrows (dark arrows)* represent the adjustable directions of slices in (a))

Table 2.1 Sample fabrication details for heterogeneous illuminations

Sample	Architecture	Fabrication method
A	Substrate/ITO/PEDOT/P3HT:PCBM/Al	Spin coating
B	Tube/ITO/PEDOT/P3HT:PCBM/Al	Dip coating
C	Substrate/ITO/PEDOT/P3HT:PCBM/Al	Dip coating

For both device types, the illumination intensity was varied to determine the performance as a function of illumination power. The case of heterogeneous illumination was simulated for the planar device by changing the area of illumination by a special mask for a given luminous power. The architecture of this tool is shown in Fig. 2.6. The active area is 0.5 cm^2 . Current voltage characteristics were collected using Keithley 236 source-measurement unit and an AM1.5 g standard Newport # 96000 Solar Simulator. The output power intensity is adjusted from 0.5 to 150 mW/cm^2 .

To test the above model three different types of organic photovoltaic cells were built. All are based on the P3HT:PCBM bulk heterojunction as described. Architectures and corresponding fabrication methods are shown in Table 2.1.

As shown above, both homogeneous and heterogeneous cases have the same functional dependence with voltage. If this is true, it will provide a simple method to study the global distribution of optical power in the OCGOPVs. First, we use an “ideal” planar device (sample A) to test the two illumination cases, shown in Fig. 2.7. As expected, both HeOI and HoOI show the same overall impact on the observed V_{oc} as average input (at the front of the device) light intensity is lowered. Specifically, the V_{oc} drops sharply when input optical intensity is lower than $\sim 10 \text{ mW/cm}^2$, which is also described by Eq. 2.3 above. In other words, the variation of the voltage is the same for every case where only a small subunit is illuminated, or part of the whole cell is illuminated. The gray curve is fitted by Eq. 2.3 in which all the parameters of devices are extracted from IV curve in terms of an iterative method [21].

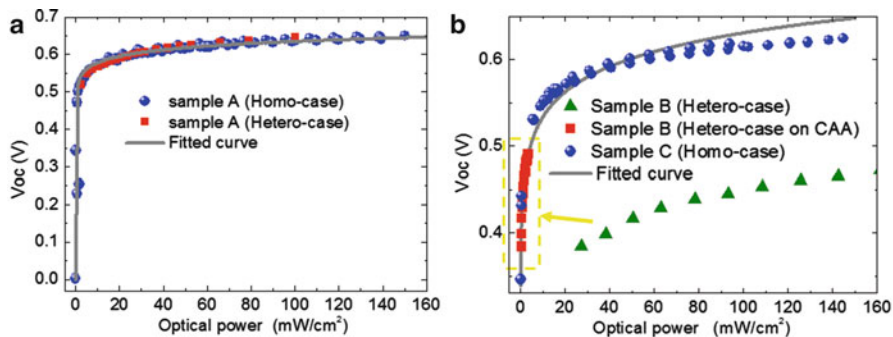


Fig. 2.7 (a) The V_{oc} versus optical intensity of sample A, which is illuminated by simulated heterogeneous variation (red square) and homogeneous variation (blue sphere) respectively. The V_{oc} versus I curves are fitted to Eq. 2.3 and shown as the grey line. (b) The V_{oc} versus optical intensity for dip coating devices. The curve with “on CAA” means the optical power of incident optical flux divided by CAA [5]. Here, the red square and green triangle are the same illumination data divided by IAA and CAA respectively

Then, we apply this principle to the tube-based cell (sample B), which was prepared by a dip coating method. In this case, the usual incident light at the front face of the OCGOPV (sample B) is homogeneous, but it will be distributed throughout the volume heterogeneously, on the inner surface as in Fig. 2.4d. In Fig. 2.7b, we plot a planar OPV (sample C, fabricated using the same dip coating procedure) together with the tube-based device. Because OCGOPVs have a very large CAA, i.e., the average optical intensity on the inner surface (CAA) is very low, the V_{oc} of the tube OPV tends to be a lower voltage than planar devices as shown in green. To determine the average optical power inside the tube, the total incident flux was divided by the total internal area of the device. This effective heterogeneous intensity (red square, B) was used to normalize the V_{oc} to intensity. This normalized V_{oc} shows the same functional behavior in the OCGOPV as homogeneous illumination does in the control device (Blue sphere, C).

To fully understand how this may modify the overall performance of the OCGOPV (the efficiency), we have also measured the filling factor and current collection for the planar device and compared it to the OCGOPV as a function of illumination intensity. Figure 2.8a shows the FF for the spin cast device (sample A, our “ideal” device), the OCGOPV (sample B) and the dip coated planar device (sample C). For the planar device fabricated with spin coating, there exists a peak in FF near $10 \text{ W}/\text{m}^2$. As is typical with such OPVs, the FF varies with the quality of the thin films, but it can be rather high (near 0.7). Generally, FF of OCGOPV is also limited by the film quality. Since dip coating was used to fabricate tube-based cell, resulting in uneven films, the FF for both the dip-coated tube structures and planar structures drop. In the case of the tube device, it is approximately reduced by 0.25. The normalized FF of OCGOPV also shows the same functional behavior as homogeneous illumination does in dip-coated planar devices (Pink line, C). In terms of Eq. 2.1, J-V is simulated to find the maximum obtainable output power

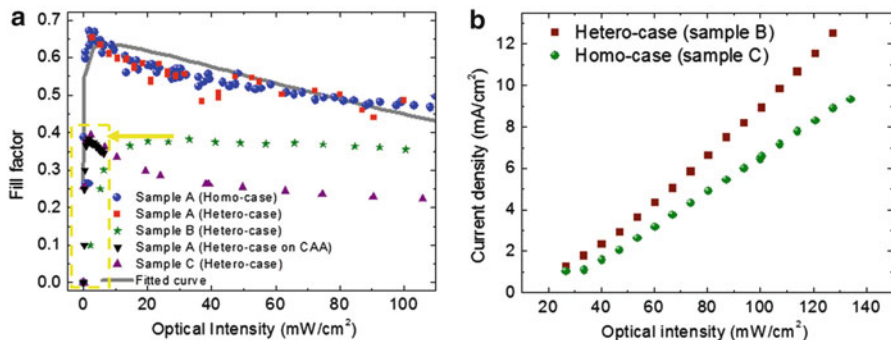


Fig. 2.8 (a) FF versus optical intensity of sample A, sample B and sample C. The *green stars* and the *black down-triangles* (in *yellow rectangle*) are the same input flux data divided by IAA and CAA respectively. The *gray line* is the fitted curve by Eq. 2.1. (b) J_{sc} versus optical intensity (IAA) of planar and OCGOPV device with architecture ITO/PEDOT/P3HT:PCBM/Al

P_m and corresponding J_m and V_m , then the FFs of different Jph are obtained as gray line in Fig. 2.8a to compare with the experiment.

On the other hand, Fig. 2.8b illustrates that the OCGOPV can transfer more light flux to current than the conventional OPV. This has been previously reported in several publications [22–24]. Moreover, this advantage is enhanced with increasing optical illumination intensity at the entrance aperture. This suggests that OCGOPVs will perform well with high illumination intensity applications such as concentrators [25–27].

We can now examine the overall result of these effects on efficiency. The efficiency as a function of incident optical illumination intensity is shown in Fig. 2.9a. For the planar cell (sample A, Blue spheres), the optimum optical intensity of the highest efficiency is near 10 mW/cm², which is far less than the AM1.5 standard solar light (100 mW/cm²) allowed for by P3HT:PCBM. That indicates the highest performance requires reducing the optical intensity. However, the tube-based cell (sample B) exhibits a monotonically increasing efficiency with optical intensity at the input aperture. This is because at the lowest values of IAA, the optical intensity within the device volume is very low. When the efficiency of the OCGOPV is scaled with the average internal illumination intensity given by CAA (shown in the yellow rectangle), the curve's shape is similar to that of the planar cell of both spin cast and dip coat at lower optical intensity but performs better than that of planar cell of same dip coating procedure (Upper angle, C). This also suggests the functional equivalence of HoOI and HeOI in OPVs, generally.

Using this “optical intensity effect,” we can predict the optimum efficiency of OCGOPVs, as a function of the geometry: ratios of the length/diameter of OCGOPV together with the ratios of bottom curvature radius to diameter (radius/diameter). Since the two fabrication procedures, dip coating film and spin coating, yield different film morphologies, we must also consider this. In Fig. 2.9b, we again use the tube-based cell as a typical case of OCGOPVs. The efficiency drops with the

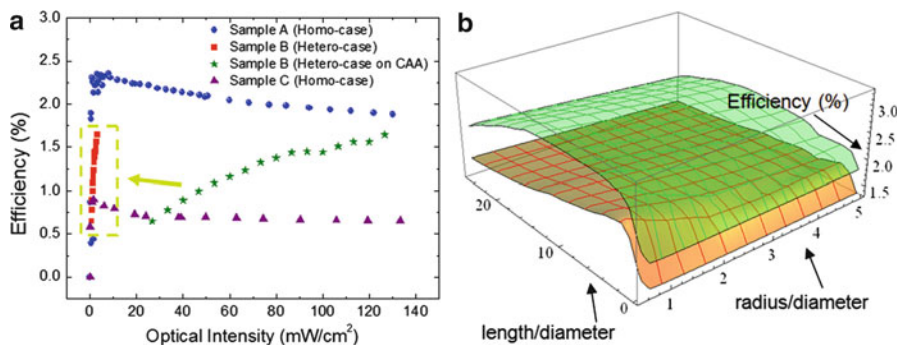


Fig. 2.9 (a). Efficiency versus optical intensity of sample A, sample B and sample C. The *green stars* and the *red squares* (in *yellow rectangle*) are the same input flux data divided by IAA and CAA respectively. (b) The simulation of efficiency versus the ratio length/diameter of tube, and the ratio of bottom curvature radius and tube diameter, is in the condition of normal incident light and for two fabrications of spin coating (*Green surface*) and dip coating (*Orange surface*). This simulation is based on an optical path method and a transfer matrix mentioned before [7, 17], and also use the experiment data from the *left figure* (a)

increase of the ratio of radius of bottom/diameter of tube, because of the reflection loss from the bottom reflector (see in Fig. 2.5c) which we have termed “the dead zone” (when this ratio $> 1/\sqrt{2}$). Moreover, the peak in the dimension of length/diameter is the combined result of current increase and voltage decrease. Longer OCGOPVs can absorb more light energy to generate a higher current density [7], but it has a negative impact on voltage. This phenomenon is simulated for both film cases. The peaks are all with relatively low optical intensity ($< 100 \text{ mW/cm}^2$) on the inner surface. Thus, the optimum design for OCGOPVs should be of length/diameter that is in the range of 1–5 and the curvature radius/diameter is between 0.5 and 0.7 for normal incidence, which the accurate ratio predictions depend on the film quality, thickness and polymer type. In Fig. 2.9b, the optimum design of tube-based geometries using P3HT:PCBM is located at length/diameter 2 and radius/diameter 0.7. This could explain why in the past, research showed that longer fiber-devices were used to reach high photocurrent but led to a lower voltage [5, 28].

In sum, this section has examined the overall effect of 3D architectures by heterogeneous illumination. Specifically, we have provided an equivalent circuit equation of OCGOPVs by revising the Shockley equation to apply to the case of optical heterogeneity within the structure. Using this approach, we have shown a functional equivalence of internal HoOI and HeOI for OPVs generally. The overall effect of optical heterogeneity on performance parameters in our model, 3D, fiber-based structure is that the V_{oc} is lowered generally as the ratio of length to diameter becomes larger. This corresponds to a large internal area of the device. J_{sc} is seen to increase substantially for large internal device areas whereas the FF is less sensitive overall. We have correlated our model calculations to experimentally obtained values in a fiber device using P3HT:PCBM absorbers. Finally, it was found that there is an optimum design to the highest efficiency for tube-based OCGOPV,

which corresponds to a length/diameter in the range of 1–5, and an optimum radius of bottom/diameter of tube lower than 0.7. These results suggest that realization of truly high performance devices utilizing polymers on 3D architectures will require new polymer systems capable of maintaining higher voltages under lower light conditions.

2.3 Dependence of Light Illumination Intensity

Fiber-based architecture, which is designed to confine the incident light in the fiber where it bounces around until it is absorbed almost completely, has been proven to not only lead to better optics performance but also a relatively thinner absorber layer reducing recombination rate. In this section, with theoretical simulation, we further demonstrate that, under high intensity of sun light ($>1,000$ suns), the fiber-based structure can dramatically enhance the efficiencies by 52.5% of planar solar cell while extending the prime working light intensity range from dozens of suns to thousands. This result shows that fiber architecture has great application potential in high concentration photovoltaic (HCPV) system.

For years, concentration photovoltaic (PVC) has attracted researchers for both very high conversion efficiencies [29–32], and dramatic reduction in the module cost for photovoltaic electricity generation by decreasing the amount of semiconductor materials needed. However, the development has been constrained by the lack of ability resisting the high intensity of light while maintaining a good performance. As we know, the efficiency will be minimized by high light intensity because efficiency equals to the product of open circuit voltage (V_{oc}), short current density (J_{sc}), and fill factor (FF), which are mainly determined by the band gap and temperature. Although light intensity is beneficial to V_{oc} [33], in contrast, high temperature resulting from very high light intensity will reduce V_{oc} , and raise the recombination rate causing lower J_{sc} . Furthermore, intense current in the equivalent circuit of a solar cell would further provide negative influence on FF and a module's lifetime. Consequently, all those facts minify the efficiency at high light intensity. However, a good PVC module should be capable of performing well at very high illumination intensity ($>1,000$ suns) and also have a large working range considering sun light intensity is volatile for different time or weather conditions. To solve this conflict, advantages of fiber-based solar cells should be considered. This optical confinement geometry has been developing in recent years [6, 7, 24, 34, 35], mostly using fiber and tube to confine light in its cavity and fully absorb light in the range of absorption. Our former work argued that the fiber-based solar cell (FBSC) performs better at higher illumination [36] due to fiber's large aspect ratio. The current active area (the wall) is much larger than the light incident area (the ends) which means the light density (incident light/active area) is low enough to avoid all the negative effects discussed above. In this work, we further examined the performance at very high illumination ($>1,000$ suns) and the universality of FBSC on different materials Fig. 2.10.

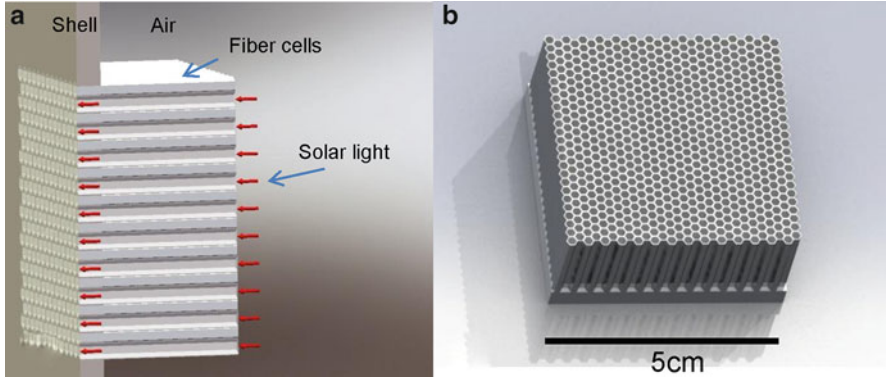


Fig. 2.10 (a) A cross section of fiber-based photovoltaic system. (b) An integrated unit of fiber-based solar cells. Red arrows represent incident light

In the past, the performances of planar solar cells based on several types of materials have been reported, including silicon [37], GaInP/GaInAs/Ge [38], CIGS [39], CZTS [40], polymer [41] and small molecular [42]. Besides, at certain incident light illumination, the performances were simulated by the following methods. First, the light distribution along the fiber cavity was obtained by a ray tracing method in Ref. [7], and the optical field in active layer is calculated in terms of Ref. [43]. By dividing fiber cell into many infinitesimal planar cells, its equivalent circuit was obtained [36]. Its photocurrent (J_{ph}), saturated current (J_s), ideal factor (n_D), and resistances of device could be extracted from the current-voltage (IV) curves with Lambert W-function [44] which is used to estimate the parameters in Poisson and continuity equations [45]. The circuit response at certain light intensity input was then simulated by finding the stable solution using Gummel's method [46]. Figure 2.11 shows the efficiencies prediction versus incident light intensity of these six materials, for both fiber cells and planar cells. All kinds of devices, regardless of being fiber-based or planar-based, have a max efficiency at a certain optimum light intensity, which are usually 100 suns for planar cells. For fiber cells, not only the prime working light intensities are increased to 593 ~ 4,830 suns for different materials, but also the max efficiencies were improved. Table 2.2 lists the best efficiencies (Eff) and corresponding light intensities (I). Remarkably, the GaInP/GaInAs/Ge triple-junction cell's efficiency reaches 43% on a fiber-based cell, which is much higher than the planar one, and a similar efficiency (40%) has been achieved at 240 suns in practice [47]. In addition, FBSC keeps 80% of the highest efficiency in a range of 7,741 suns at very high light intensity. Compared to only 35.5 suns range of planar cells at a relatively low light intensity, FBSC has much better compatibility, especially for concentrating solar power system. Furthermore, it is surprising that even organic cells like polymer and small molecular can both reach 10% efficiency, which is a general critical value to realize industrial production.

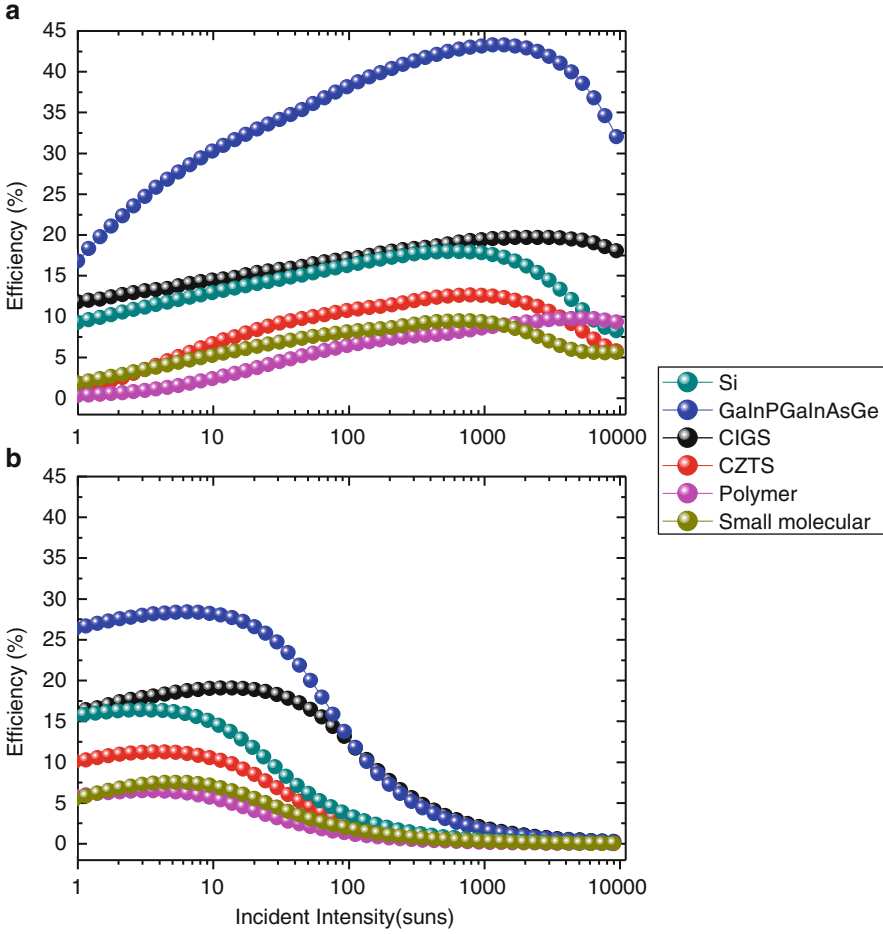


Fig. 2.11 Efficiencies versus incident intensity for fiber-based solar cells in (a) and planar solar cells in (b)

Figure 2.12 further shows the efficiency dependence on incident angle and aspect ratio for fiber cells at 1,000 suns light intensity. It generally reveals that the optimum incident angles are lower than 40° , and become smaller along with the increase of aspect ratio, because the total light flux passing through the fiber is proportional to the cosine function of incident angle, such that more energy will be wasted before entering the fiber's cavity for bigger angles. In addition, although longer fiber is beneficial to the absorption, meanwhile, the larger CCA leads to sharp Voc dropping off [36], therefore giving the aspect ratios an optimum value. This provides a concept of designing the architecture of fiber-based solar used in a concentrator system.

Table 2.2 Max efficiencies (Eff) and corresponding light intensity (I) for six materials based on fiber cells and planar cells

	Si	GaInP/GaInAs/Ge	CIGS	CZTS	Polymer	Small molecular
Fiber cells						
Eff (%)	18.0	43.3	19.7	12.6	9.8	9.5
I (suns)	593	1,272	2,479	790	4,830	653
R _{work} (suns)	2,970	7,741	9,381	3,239	8,922	2,193
	(28 ~ 2,999)	(37 ~ 7,779)	(31 ~ 9,412)	(60 ~ 3,299)	(490 ~ 9,412)	(60 ~ 2,257)
Planar cells						
Eff (%)	16.4	28.4	19.3	11.3	7.5	6.5
I (suns)	3	6	13	4	5	3
R _{work} (suns)	14.4	35.5	76.5	16.2	15.4	10.9
	(0.2 ~ 14.6)	(0.2 ~ 35.7)	(0.2 ~ 76.7)	(0.5 ~ 16.7)	(1.3 ~ 16.7)	(0.5 ~ 11.4)

Note: R_{work} represents working range that device has efficiency higher than 80% max efficiency, and with the start and end light intensity in brackets

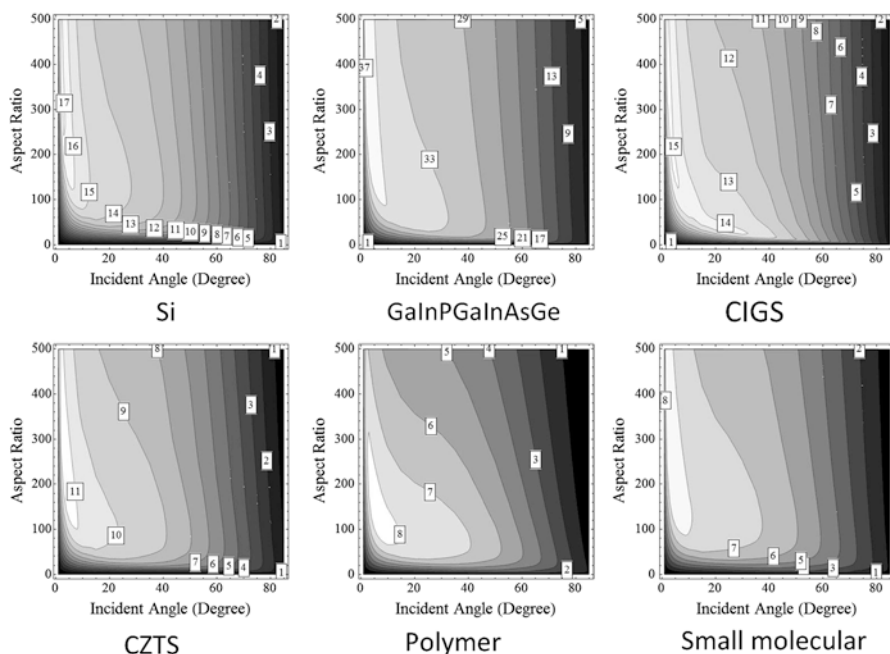


Fig. 2.12 Efficiencies (%) versus incident angle and aspect ratio for fiber-based solar cells based Si, GaInPGaInAsGe, CIGS, CZTS, polymer and small molecular

In sum, fiber-based solar cell has an excellent performance at very high light intensity by increasing the max efficiency and prime working light intensity as well as extending the working range hundreds of times of the planar cells. Also, all those advantages are proved to be valid for six types of solar cells, especially for GaInP/GaInAs/Ge solar cell, which is mostly used in HCPV system nowadays. Therefore, this architecture may provide a brand new method and different thought to clearing the obstacles facing the development of a CPV system.

References

1. Y. Li, M. Wang, H. Huang, W. Nie, Q. Li, E.D. Peterson, R. Coffin, G. Fang, D.L. Carroll, Influence on open-circuit voltage by optical heterogeneity in three-dimensional organic photovoltaics. *Phys. Rev. B*. **84**(8), 085206
2. R. Hausermann, E. Knapp, M. Moos, N.A. Reinke, T. Flatz, B. Ruhstaller, Coupled optoelectronic simulation of organic bulk-heterojunction solar cells: Parameter extraction and sensitivity analysis. *J. Appl. Phys.* **106**, 104507 (2009)
3. D.W. Sievers, V. Shrotriya, Y. Yang, Modeling optical effects and thickness dependent current in polymer bulk-heterojunction solar cells. *J. Appl. Phys.* **100**, 114509 (2006)

4. Y.M. Nam, J. Huh, W.H. Jo, Optimization of thickness and morphology of active layer for high performance of bulk-heterojunction organic solar cells. *Sol. Energ. Mat.Sol. C*, **94**, 1118–1124 (2010)
5. Y. Li, E.D. Peterson, H. Huang, M. Wang, D. Xue, W. Nie, W. Zhou, D.L. Carroll, Tube-based geometries for organic photovoltaics. *Appl. Phys. Lett.* **96**, 243505 (2010)
6. Y. Li, W. Nie, J. Liu, A. Partridge, D.L. Carroll, The optics of organic photovoltaics: Fiber-based devices. *IEEE J. Sel. Top. Quant. Elect.* **16**, 1827–1837 (2010)
7. Y. Li, W. Zhou, D. Xue, J. Liu, E.D. Peterson, W. Nie, D.L. Carroll, Origins of performance in fiber-based organic photovoltaics. *Appl. Phys. Lett.* **95**, 203503 (2009)
8. R.H. Bube, A.L. Fahrenbruch, *Advances in Electronics and Electron Physics* (Academic, New York, 1981), p. 163
9. A. Cheknane, H.S. Hilal, F. Djeflal, B. Benyoucef, J.P. Charles, An equivalent circuit approach to organic solar cell modelling. *Microelectron. J.* **39**, 1173–1180 (2008)
10. A. Shah, P. Torres, R. Tscharnner, N. Wyrsh, H. Keppner, Photovoltaic technology: The case for thin-film solar cells. *Science* **285**, 692–698 (1999)
11. A.L. Fahrenbruch, J. Aranovich, *Solar Energy Conversion* (Springer, New York, 1979), p. 257
12. B.P. Rand, D.P. Burk, S.R. Forrest, Offset energies at organic semiconductor heterojunctions and their influence on the open-circuit voltage of thin-film solar cells. *Phys. Rev. B*, **75**, 115327 (2007)
13. K. Vandewal, K. Tvingstedt, A. Gadisa, O. Inganäs, J.V. Manca, On the origin of the open-circuit voltage of polymer-fullerene solar cells. *Nat. Mater.* **8**, 904–909 (2009)
14. G. Li, V. Shrotriya, J. Huang, Y. Yao, T. Moriarty, K. Emery, Y. Yang, High-efficiency solution processable polymer photovoltaic cells by self-organization of polymer blends. *Nat. Mater.* **4**, 864–868 (2005)
15. Y. Li, Y. Zou, Conjugated polymer photovoltaic materials with broad absorption band and high charge carrier mobility. *Adv. Mater.* **20**, 2952–2958 (2008)
16. A. Pivrikas, G. Juscaraonka, A.J. Mozer, M. Scharber, K. Arlauskas, N.S. Sariciftci, H. Stubb, R.O. Sterbacka, Bimolecular recombination coefficient as a sensitive testing parameter for low-mobility solar-cell materials. *Phys. Rev. Lett.* **94**, 176806 (2005)
17. L.A.A. Pettersson, L.S. Roman, O. Inganäs, Modeling photocurrent action spectra of photovoltaic devices based on organic thin films. *J. Appl. Phys.* **86**, 487–496 (1999)
18. F. Monestier, J.-J. Simon, P. Torchio, L. Escoubas, F. Flory, S. Bailly, R. de Bettignies, S. Guillerez, C. Defranoux, Modeling the short-circuit current density of polymer solar cells based on P3HT:PCBM blend. *Sol. Energ. Mat. Sol. C*, **91**, 405–410 (2007)
19. B.G. Wei, Study of parallel DC power. *Tech. Phys. Teach.* **16**, 17–18 (2008)
20. D.I. Cartwright, M.J. Field, Refinement of arithmetic mean geometric mean inequality. *P. Am. Math. Soc.* **71**, 36–38 (1978)
21. K.I. Ishibashi, Y. Kimura, M. Niwano, An extensively valid and stable method for derivation of all parameters of a solar cell from a single current–voltage characteristic. *J. Appl. Phys.* **103**, 094507 (2008)
22. J.W. Liu, M.A.G. Namboothiry, D.L. Carroll, Optical geometries for fiber-based organic photovoltaics. *Appl. Phys. Lett.* **90**, 133515 (2007)
23. M.R. Lee, R.D. Eckert, K. Forberich, G. Dennler, C.J. Brabec, R.A. Gaudiana, Solar power wires based on organic photovoltaic materials. *Science* **324**, 232–235 (2009)
24. B. O'Connor, K.P. Pipe, M. Shtein, Fiber based organic photovoltaic devices. *Appl. Phys. Lett.* **92**, 193306 (2008)
25. M.J. Currie, J.K. Mapel, T.D. Heidel, S. Goffri, M.A. Baldo, High-efficiency organic solar concentrators for photovoltaics. *Science* **321**, 226–228 (2008)
26. C. Dominguez, I. Anton, G. Sala, Solar simulator for concentrator photovoltaic systems. *Opt. Express* **16**, 14894–14901 (2008)
27. K. Omer, H. Baruch, A.K. Eugene, M.G. Jeffrey, High-flux characterization of ultrasmall multijunction concentrator solar cells. *Appl. Phys. Lett.* **91**, 064101 (2007)

28. H. Huang, Y. Li, M. Wang, W. Nie, W. Zhou, E.D. Peterson, J. Liu, G. Fang, D.L. Carroll, Photovoltaic-thermal solar energy collectors based on optical tubes. *Sol. Energ.* **85**, 450–454 (2011)
29. L.W. James, R.L. Moon, Gaas concentrator solar cell. *Appl. Phys. Lett.* **26**, 467–470 (1975)
30. R. Sinton, Y. Kwark, R.M. Swanson, 23-percent efficient Si point contact concentrator solar-cell. *IEEE T. Electron. Dev.* **32**, 2553–2554 (1985)
31. M.A. Green, A. Ho-Baillie, Forty three per cent composite split-spectrum concentrator solar cell efficiency. *Prog. Photovoltaics* **18**, 42–47 (2010)
32. J.S. Ward, K. Ramanathan, F.S. Hasoon, T.J. Coutts, J. Keane, M.A. Contreras, T. Moriarty, R. Noufi, A 21.5% efficient Cu(In,Ga)Se-2 thin-film concentrator solar cell. *Prog. Photovoltaics* **10**, 41–46 (2002)
33. S.R. Cowan, A. Roy, A.J. Heeger, Recombination in polymer-fullerene bulk heterojunction solar cells. *Phys. Rev. B.* **82**, 245207 (2010)
34. B. Weintraub, Y.G. Wei, Z.L. Wang, Optical fiber/nanowire hybrid structures for efficient three-dimensional dye-sensitized solar cells. *Angew. Chem. Int. Edit.* **48**, 8981–8985 (2009)
35. A. Gagliardi, M.A.D. Maur, A. Di Carlo, Theoretical investigation of a dye solar cell wrapped around an optical fiber. *IEEE J. Quantum. Elect.* **47**, 1214–1221 (2011)
36. Y. Li, M. Wang, H. Huang, W. Nie, Q. Li, E.D. Peterson, R. Coffin, G. Fang, D.L. Carroll, Influence on open-circuit voltage by optical heterogeneity in three-dimensional organic photovoltaics. *Phys. Rev. B.* **84**, 085206 (2011)
37. S.B. Ghazati, A.U. Ebong, C.B. Honsberg, S.R. Wenham, Improved fill-factor for the double-sided buried-contact bifacial silicon solar cell. *Sol. Energ. Mat. Sol. C.* **51**, 121–128 (1998)
38. S. Roensch, R. Hoheisel, F. Dimroth, A.W. Bett, Subcell I-V characteristic analysis of GaInP/GaInAs/Ge solar cells using electroluminescence measurements. *Appl. Phys. Lett.* **98**, 251113 (2011)
39. NREL, Manufacturing-friendly advance seen in CIGS solar cell processing, NREL Highlights, NREL/FS-5200-51412 (2011)
40. T.K. Todorov, K.B. Reuter, D.B. Mitzi, High-efficiency solar cell with earth-abundant liquid-processed absorber. *Adv. Mater.* **22**, E156 (2010)
41. W. Nie, C.M. MacNeill, Y. Li, R.E. Noffle, D.L. Carroll, R.C. Coffin, A soluble high molecular weight copolymer of benzo[1,2-b:4,5-b']dithiophene and benzoxadiazole for efficient organic photovoltaics. *Macromol. Rapid. Comm.* (2011) n/a-n/a
42. M. Riede, C. Urich, J. Widmer, R. Timmreck, D. Wynands, G. Schwartz, W.M. Gnehr, D. Hildebrandt, A. Weiss, J. Hwang, S. Sundarraj, P. Erk, M. Pfeiffer, K. Leo, Efficient organic tandem solar cells based on small molecules. *Adv. Funct. Mater.* **21**, 3019–3028 (2011)
43. Y. Li, H. Huang, M. Wang, W. Nie, W. Huang, G. Fang, D.L. Carroll, Spectral response of fiber-based Photovoltaics. *Sol. Energ. Mat. Sol. C.* (2011 in press)
44. A. Jain, A. Kapoor, A new method to determine the diode ideality factor of real solar cell using Lambert W-function. *Sol. Energ. Mat. Sol. C.* **85**, 391–396 (2005)
45. L.J.A. Koster, E.C.P. Smits, V.D. Mihailetschi, P.W.M. Blom, Device model for the operation of polymer/fullerene bulk heterojunction solar cells. *Phys. Rev. B.* **72**, 085205 (2005)
46. H.K. Gummel, A self-consistent iterative scheme for one-dimensional steady state transistor calculations. *IEEE T. Electron. Dev.* **11**, 455–465 (1964)
47. R.R. King, D.C. Law, K.M. Edmondson, C.M. Fetzer, G.S. Kinsey, H. Yoon, R.A. Sherif, N.H. Karam, 40% efficient metamorphic GaInP/GaInAs/Ge multijunction solar cells. *Appl. Phys. Lett.* **90**(18), 183516 (2007), AIP

Three Dimensional Solar Cells Based on Optical
Confinement Geometries

Li, Y.

2013, XXX, 154 p., Hardcover

ISBN: 978-1-4614-5698-8